Touchless spacecraft potential sensing using energetic electron beams and active photoemission

Álvaro Romero-Calvo[1], Kaylee Champion[2], and Hanspeter Schaub[3]

***Abstract*—Ultraviolet lasers are proposed as a replacement for low-energy electron beams to induce the emission of secondary electrons in touchless spacecraft potential sensing technologies. Theoretical considerations show that the measurement process becomes significantly less sensitive to the electrostatic environment and leads to more robust, controllable systems. Lasers could be employed in combination with high-energy electron beams to independently induce the emission of photoelectrons and x-rays close to their optimum operational points. This approach would enable hybrid photoelectron and x-ray potential sensing methods with enhanced detectability and sensing accuracy. Applications in touchless potential sensing, charge control, and material characterization are identified.**

I. Introduction

Novel active sensing methods have been recently proposed to touchlessly sense the electrostatic potential of non-cooperative objects in Geosynchronous Equatorial Orbit (GEO) and deep space. Such approaches make use of a positively charged servicing craft that directs an electron beam at the object of interest so that low-energy secondary electrons [1, 2] and x-rays [3, 4] are emitted from its surface. The servicer measures the incoming signals and, knowing its own potential, infers that of the target. This information can be employed to compensate for electrostatic perturbations in close-proximity multi-spacecraft operations [5, 6], minimize the risk of electrostatic discharge during rendezvous, control spacecraft formations [7], and detumble [8] or reorbit [9–13] space debris by means of electrostatic forces, among others.

Analytical and experimental studies have shown that the combined measurement of secondary electrons and x-rays enhances the robustness and accuracy of the sensing process [14, 15]. However, the physics of each problem are not favorable to the simultaneous generation of these signals: while secondary electrons are produced at moderate electron beam energies [16], the generation of x-rays is favored by energetic particle impacts [3]. In addition, low-energy electron beams are steered in the presence of the inhomogeneous electrostatic field generated by the servicer-target system, increasing the uncertainty of the problem [2, 15]. From a technical perspective, it would be convenient to develop a sensing procedure that uncouples both mechanisms and optimizes the generation and control of secondary electrons and x-rays while minimizing the current fluxes imparted on the target.

1: Aerospace Engineering Sciences Department, University of Colorado at Boulder, (email: alvaro.romerocalvo@colorado.edu)
2: Aerospace Engineering Sciences Department, University of Colorado at Boulder, (email: kach7227@colorado.edu)
3: Aerospace Engineering Sciences Department, University of Colorado at Boulder, (email: Hanspeter.Schaub@colorado.edu)

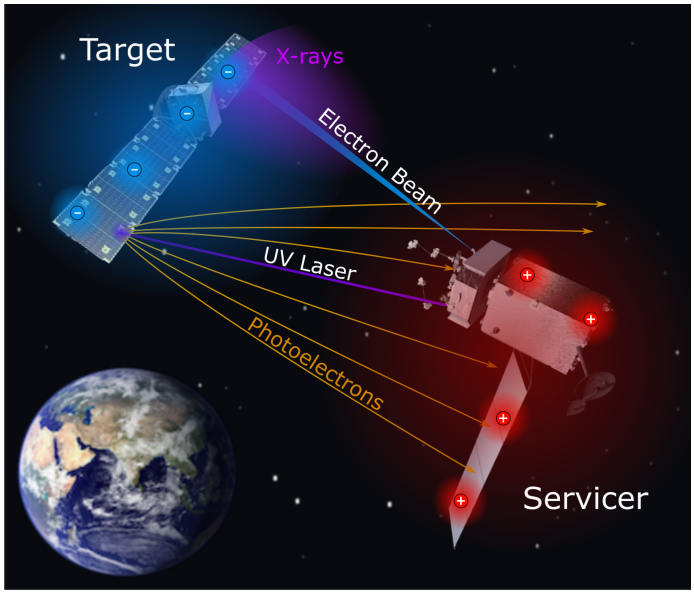

Fig. 1. Conceptual representation of the combined photoelectron and x-ray generation processes.

The simultaneous employment of ultraviolet (UV) lasers and high-energy electron beams is proposed in this work to excite the emission of photoelectrons and x-rays in non-cooperative GEO objects. Figure 1 shows a conceptual representation where both systems operate independently and impact (if needed) different areas of the target. Major sources of uncertainty are eliminated with this approach due to the high directivity of quasi-relativistic electron beams and the independence of ultraviolet photons from the complex electrostatic environment. In addition, independently controlled positive (photoelectrons) and negative (electron beam) currents are added to the target spacecraft charge balance, enabling a promising new method to touchlessly sense the electrostatic potential of a GEO object without changing its equilibrium state.

The theoretical background of the problem is reviewed in Sec. II, followed by a critical analysis of the secondary electron and x-ray touchless potential sensing methods in Sec. III. The technical relevance of the active photoemission approach is addressed in Sec. IV, where some of the applications enabled by the simultaneous use of UV lasers and quasi-relativistic electron beams in spacecraft charging scenarios are discussed.

II. Theoretical Background

In addition to fundamental spacecraft charging concepts, an excellent review of which can be found in Ref. 16, the touchless spacecraft potential sensing methods discussed in this work rely on the emission secondary and backscattered electrons, photoelectrons, and x-rays. This section provides an overview of such interactions.

A. Secondary Electron Emission

Secondary electrons are emitted from the surface of a given material when impacted by a primary electron or ion. The *secondary electron yield* δ determines the probability of emission of secondaries per impinging particle. This value depends on the incidence energy E of the primary particle in a relation that can be roughly approximated by the Sanders and Inouye yield model

$$\delta(E,0) = c\left[e^{-E/a} - e^{-E/b}\right], \tag{1}$$

where $a = 4.3E_{\text{max}}$, $b = 0.367E_{\text{max}}$, and $c = 1.37\delta_{\text{max}}$ [17]. The parameters E_{max} and δ_{max} define the maximum yield point and characterize the response of the surface. Alternative models have been proposed and an excellent review of them can be found in Sec. 2.2 of Ref. [18].

The emission of secondaries is also dependent on the incidence angle ϕ of the primary particle (with $0°$ for normal incidence). Darlington and Cosslett propose the relation [19]

$$\delta(E,\phi) = \delta(E,0)e^{\beta_s(1-cos\phi)}, \tag{2}$$

with $\delta(E,0)$ being the secondary electron yield obtained from Eq. 1, and

$$\beta_s = e^{\zeta}, \tag{3a}$$

$$\zeta = 0.2755(\xi - 1.658) - \left\{[0.2755(\xi - 1.658)]^2 + 0.0228\right\}^{1/2}, \tag{3b}$$

$$\xi = \ln\left(E/E_{\text{max}}\right), \tag{3c}$$

empirical factors proposed by Laframboise and Kamitsuma [16].

The energy E_s of a secondary electron with respect to the vacuum level is of the order of a few eV and follows a characteristic distribution with a peak at one third of the work function φ of the material. The Chung-Everhart normalized probability density function

$$f(E_s) = \frac{6\varphi^2 E_s}{(E_s + \varphi)^4} \tag{4}$$

is commonly employed in this context [20].

The angular distribution of secondary electrons follows approximately Lambert's cosine law and is nearly independent of the angle of incidence of the impinging particle [21].

B. Backscattered electrons

Backscattered electrons are primary electrons reflected off the target surface [16]. Although they do not play a central role in the touchless measurement of target spacecraft potentials, they can influence the magnitude and source regions of secondary electron fluxes.

Following the same approach as with secondary electrons, it is possible to define the backscattered electron yield η as the probability of reflection of an incoming electron. For sufficiently high impact energies, η depends on the atomic number Z and the impact angle ϕ, and is virtually independent of the primary electron energy E. In this regime, Everhart proposes the model [22]

$$\eta(Z,0) = \frac{a - 1 + 0.5^a}{a + 1}, \tag{5}$$

with $a(Z) = 0.045Z$ being an experimentally fitted parameter. The minimum electron energy (in eV) that makes this approach valid is shown to be

$$E_{\text{min}} \geq 13.7Z^{4/3}\tan\left(\theta/2\right), \tag{6}$$

with $180° - \theta$ being the deflection angle of the electron in the material. To establish this value, Everhart suggests using $\theta = 45°$.

Darlington and Cosslett's model can also be employed to compute the influence of the incidence angle of the primary electrons on the generation of backscattered electrons, resulting in [19]

$$\eta(Z,\phi) = \eta(Z,0)e^{\beta_b(1-cos\phi)}, \tag{7}$$

with $\eta(Z,0)$ being the backscattered electron yield obtained from Eq. 5, and where

$$\beta_b = 7.37Z^{-0.56875}, \tag{8}$$

is an empirical factor proposed by Laframboise and Kamitsuma [16].

C. Photoelectron Emission

Photoelectrons can be regarded as a particular case of secondary electrons for which the impinging particle is a photon. The probability of emission of a photoelectron per collision is determined by the photoelectric yield [16]

$$Y[\omega,\phi,R] = Y^*[\omega,\phi][1 - R], \tag{9}$$

where $Y^*[\omega,\phi]$ is the yield per absorbed photon, ω is the photon energy, ϕ is in this case the photon incidence angle, and $R(\omega,\phi,\sigma)$ is the surface reflectance, which depends on the photon energy, incidence angle, and root mean square surface roughness σ. The incidence angle effect on the yield is of the form [23]

$$Y^*[\omega,\phi] \approx \frac{Y^*[\omega,0]}{\cos\phi}, \tag{10}$$

but since $1 - R(\omega,\phi,\sigma)$ also has the approximate dependence [24, 25]

$$1 - R(\omega,\phi,\sigma) \approx [1 - R(\omega,0,\sigma)]\cos\phi, \tag{11}$$

both $\cos\phi$ terms cancel in Eq. 9. Therefore, $Y[\omega, R]$ is not, in first-order approximation, a function of the photon incidence angle [16].

The total reflectance is expressed as the sum of specular (R_s) and diffuse (R_d) reflectances

$$R(\omega, 0, \sigma) = R_s(\omega, 0, \sigma) + R_d(\omega, 0, \sigma), \tag{12}$$

which are defined as [26]

$$R_s(\omega, 0, \sigma) = R_0(\omega) \exp\left[\frac{-(4\pi\sigma)^2}{\lambda^2}\right], \tag{13}$$

$$R_d(\omega, 0, \sigma) = R_0(\omega)\frac{(4\pi\sigma)^2}{\lambda^2}, \tag{14}$$

with $R_0(\omega)$ being the normal reflectance of a perfectly smooth surface of the impacted material, $\lambda = hc/\omega$ the photon wavelength, h Planck's constant, and c the speed of light. The ratio of diffuse to specular reflectances is

$$\frac{R_d}{R_s} = \frac{(4\pi\sigma)^2}{\lambda^2} \exp\left[\frac{(4\pi\sigma)^2}{\lambda^2}\right], \tag{15}$$

implying that for small wavelength and large surface roughness the diffuse term is the major contributor to the total reflectance. Reflected photons experience negligible energy variations [25] and can generate photoelectrons at different surfaces.

Since photoelectrons are a particular case of secondary electrons, their angular emission distribution follows approximately Lambert's cosine law. Their emission energy, however, follows the relation

$$E_p = \omega - \varphi. \tag{16}$$

The Ly-α line (121.6 nm, 10.2 eV) is dominant in the solar spectrum, and hence most photoelectrons will be generated with about 5 to 6 eV. Therefore, a small positive spacecraft potential will act as a potential dwell and prevent their release [27].

D. X-ray emission

X-ray-based spacecraft potential sensing applications are mainly concerned with atomic bremsstrahlung spectra emitted by thick targets excited by mildly relativistic 10-60 keV electrons [3]. As with secondary electron emission, it is possible to define an x-ray emission yield that compares the energy radiated by photons with the energy deposited by electrons. Kulenkopff proposes the simplified formulation

$$\epsilon(E, Z) = a\left(ZE + 16.3Z^2\right), \tag{17}$$

where $a \approx 1.2 \cdot 10^{-9}$ is an empirical constant [28]. The x-ray yield is thus proportional to E and Z^2.

A variety of models can be used to simulate the bremsstrahlung spectrum [29]. In particular, the empirical fit presented in Ref. 30 has been successfully employed spacecraft potential sensing studies [31]. However, Kramer's law [32]

$$dI(\lambda) = \frac{K}{\lambda^2}\left(\frac{\lambda}{\lambda_{\text{min}}} - 1\right) d\lambda, \tag{18}$$

that neglects the absorption of x-rays by the material or electron backscattering (effects that can be important for thick targets), provides sufficient insight into the shape of the spectrum. In this expression, $dI(\lambda)$ is the emitted intensity over wavelength interval $d\lambda$, K is a constant proportional to the atomic number, and λ_{min} is the shortest emitted wavelength. Since the photon energy is bounded by the energy of the impacting electron through $\omega < E$, the minimum photon wavelength is determined by Planck's equation through

$$\lambda_{\text{min}} = \frac{hc}{E}. \tag{19}$$

The angular distribution of x-rays can be roughly approximated as [28]

$$P(\phi_r) \propto \frac{\sin^2\phi_r}{\left[1 - \beta\cos(\phi_r)\right]^5}, \tag{20}$$

with ϕ_r being the angle relative to the electron impact trajectory, and β the ratio between the electron velocity and the speed of light.

E. Material properties

The secondary electron, x-ray, and photoelectron emission processes depend on a series of surface properties that must be characterized in a laboratory environment. This section presents standard values for a range of space materials.

1) Secondary electron emission: The parameters δ_{max} and E_{max} define the shape of the Sanders and Inouye secondary electron yield curve and its angular dependence according to the Darlington and Cosslett model, while the work function φ of the conductive material determines the Chung-Everhart secondary electron energy distribution. The electron affinity χ defines the energy separation between the lowest possible state for any excited electron in a dielectric material and the vacuum level, and it may be used in place of the work function when analyzing dielectrics [33]. Table I reports these values together with the first (E_1) and second (E_2) crossover points (for which $\delta = 1$) for selected materials [33, 34].

Although the Sanders and Inouye yield model is adopted in this work, some materials exhibit high-energy yields that may be significantly larger than those predicted by Eq. 1. For instance, gold has a yield of ~0.7 at ~20 keV [35].

2) Backscattered electron yield: Equation 5 provides a good estimation of the backscattered electron yield for energies above the limit given by Eq. 6 as a function of the Z values listed in Table I. However, it is also important to characterize how $\eta(E, 0)$ evolves for $E < E_{\text{min}}$. Figure 2

TABLE I
EMISSION PARAMETERS FOR SELECTED MATERIALS [33, 34].

Material	Z	φ/χ [eV]	δ_{max}	E_{max} [eV]	E_1 [eV]	E_2 [eV]
Aluminum	13	4.20	1.0	300	300	300
Gold	79	5.47	1.4	800	150	>2000
Copper	29	5.10	1.3	600	200	1500
Iron	26	4.67	1.3	400	120	1400
Kapton	4.7	5.8	1.67	280	50	750
Teflon	3.8	4.1	2.4	350	50	180

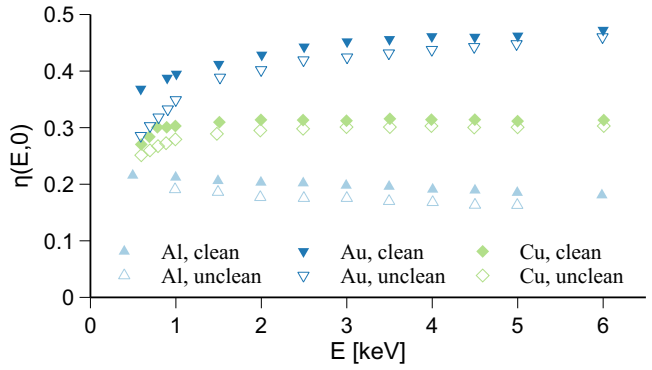

Fig. 2. Backscattered electron yield for selected materials as a function of the impacting electron energy [36].

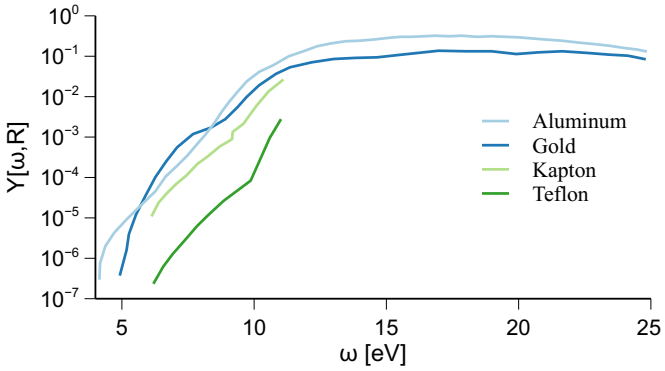

Fig. 3. Photoelectric yield for selected materials as a function of the impacting photon energy [37–39]

depicts the yield values below 6 keV for clean (ion bombarded) and unclean samples of aluminum, gold, and copper from Ref. 36. As expected, clean and unclean values converge and the measurements stabilize as E grows. The backscattered electron yield ranges between 20% and 50%, highlighting the importance of this effect for the applications considered in this work.

3) Photoelectric yield: The photoelectric yield $Y[\omega, R]$ depends on several properties, including surface roughness, reflectance, and work function [37], which motivate its characterization in laboratory environments. Results for aluminum, gold, Kapton, and Teflon are presented in Fig. 3 as a function of the photon impact energy. Kapton and Teflon are backed by silver [38]. In the case of aluminum and gold, the yield increases with the impinging photon energy until it reaches a plateau at 10^{-1} and about 12 eV.

4) Normal reflectance: Similarly to the photoelectric yield, the normal reflectance of a perfectly smooth surface should be characterized experimentally. Figure 4 shows the value of $R_0(\omega)$ for selected materials as a function of the impinging photon energy [34]. Kapton is backed by aluminum, as it would be on multi-layer insulators [39], and Teflon is backed by silver. The reflectance decreases with the photon energy for all materials, but aluminum remains highly reflective until ∼15 eV.

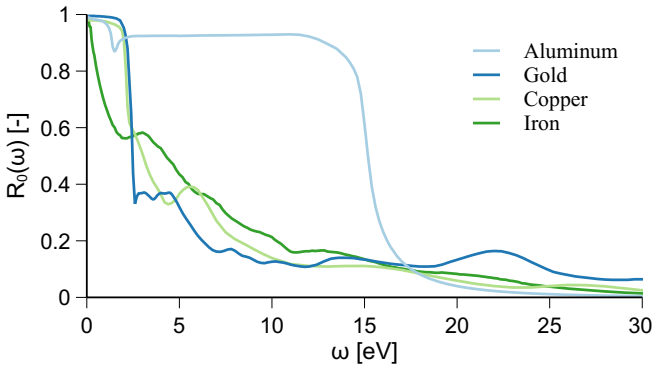

Fig. 4. Normal reflectance for selected materials as a function of the impacting photon energy [34, 39, 40].

III. Critical Analysis of Previous Methods

The surface properties listed in Sec. II-E are generally obtained in a controlled laboratory environment with samples that have been previously cleaned with ion sources. Since even the slightest change in surface conditions can alter these values [41–44], surface properties can degrade significantly after a prolonged exposition to the GEO environment [45]. This adds a layer of uncertainty that must be accounted for in the touchless potential sensing strategies described in previous works.

In the electron-based touchless potential sensing method the release of secondary electrons at the target is induced by a low-energy electron beam generated at the servicer [1]. The use of low-energy beams is motivated by the rapid decay of the secondary electron yield $\delta(E, \phi)$, described by Eq. 1, after the peak δ_{max} located at $E_{\text{max}} < 1000$ eV (see Table I). Low-energy primary electrons are susceptible to the complex electrostatic environment around the two-spacecraft system, adding further uncertainty to the steering and expansion of the electron beam [15]. However, as previously mentioned, at high energy the secondary electron yield may be modeled using an extended power law instead of Eq. 1. This results in higher yields than expected at energy greater than E_{max}, which may allow high energy beams that are less susceptible to the ambient electrostatic environment to be utilized [18, 35]. Further investigations are necessary to determine the feasibility of this in the context of the electrostatic tractor. In addition to δ_{max} and E_{max}, the secondary electron flux also depends on the backscattered electron yield $\eta(E, \phi)$. Even though the degradation of these parameters with respect to laboratory conditions can significantly impact the charge balance and secondary electron flux magnitude in the target, the spatial detectability of secondaries in a complex electrostatic environment is generally considered to remain unaffected [2]. If further assurance is desired, the use of a collimator may be used to limit the sources of secondary electrons entering the detector and reject SEE emissions from background surfaces (see e.g. the Electron Drift Experiment for the Magnetospheric Multiscale Mission [46]).

The operational conditions for the x-rays method, described in Refs. [3, 4], are the exact opposite of the electron-based

method. As shown by Eq. 17, the emission of x-rays is enhanced for high-energy primary electron impacts, while the emission of secondary electrons is minimized (see Eq. 1). The higher electron velocity also increases its gyroradius, leading to quasi-rectilinear (hence, easily predictable) trajectories. Finally, the backscattered electron yield converges to the value given by Eq 5, which remains relatively constant with surface degradation, as shown in Fig. 2.

Although the x-ray sensing method is particularly robust to changes in the geometry of the problem [4], it is significantly less accurate than the secondary electron method [14], which in turn exhibits large sensitivities to the electrostatic environment [2]. Both approaches are therefore complementary. However, the use of low-energy electron beams in the secondary electron method complicates the measurement process and makes it particularly sensitive to material uncertainties. A possible solution is proposed in the next section.

IV. Active photoemission strategy

High-energy ultraviolet lasers could be used as a replacement of low-energy electron beams for secondary electron generation. Unlike the latter, the former are insensitive to the electrostatic environment. For sufficiently high photon impact energies the photoelectric yield $Y[\omega, R]$ becomes almost insensitive to surface contamination [38], and the reflectance $R(\omega, \phi, \sigma)$ is reduced (see Fig. 4). Knowledge of the target material leads to a significantly more predictable system in comparison with secondary electron and x-ray methods. Some of the applications that benefit from this approach are subsequently described.

A. Touchless potential sensing

The use of ambient-induced photoelectrons for remote potential sensing determination has been demonstrated in Ref. 47 employing UV light sources in the ECLIPS vacuum chamber [48]. As previously noted, active photoemission makes use of UV lasers to release photoelectrons with energies of the order of few electronvolts (see Eq. 16). The electrons are then accelerated by the electrostatic environment and reach the servicer with an energy that is approximately equal to the potential difference between the crafts. A Retarding Potential Analyzer (RPA) is employed to characterize this flux and determine the energy of incoming electrons. Knowing the potential of the servicer, that of the target is finally determined.

The active photoemission approach can be employed alone or in combination with high-energy electron beams. However, the standalone implementation risks increasing the target potential by releasing photoelectrons, eventually preventing their emission. In addition, a concentrated laser beam may locally charge the target and shift its potential [18, 35], inducing further measurement errors. A trade-off study between laser power and RPA sensitivity should be carried out to identify the best operational regime. Close proximity operations may benefit from the accuracy of this method and the compactness of the hardware involved.

B. Charge control

The decoupling of the x-ray and secondary electron generation processes and the net negative and positive current fluxes that they respectively impart on the target brings the opportunity of measuring the target potential without significantly altering the measurement. To do so, the positive and negative current fluxes must be balanced.

The number of UV photons impacting the target per second can be approximated as

$$j_{\text{ph}} = \frac{P_l}{\omega_l}, \tag{21}$$

with P_l and ω_l denoting the laser power and laser photon energy, respectively. The photoelectron current is then

$$J_{\text{ph}} = Y[\omega_l, R] j_{\text{ph}}. \tag{22}$$

Similarly, the flux of high-energy electrons is

$$j_e = \frac{I_b}{q_e}, \tag{23}$$

where I_b is the current of the electron beam and q_e is the elemental charge. For beam energies E_b of the order of 10s of keV and for most materials, $\delta(E, 0) \ll \eta(Z, E, \phi)$ and the flux of incoming electrons becomes

$$J_{\text{e}} = [1 - \eta(Z, \phi)] j_e. \tag{24}$$

If follow-up interactions produced by backscattered electrons and reflected photons are ignored, the condition for neutral charging is obtained by equaling Eqs. 22 and 24, resulting in

$$I_b = \frac{q_e}{\omega_l} \frac{Y[\omega_l, R]}{[1 - \eta(Z, 0, \phi)]} P_l, \tag{25}$$

which gives the electron beam current I_b required to balance, in first order approximation, the charge induced by a laser with power P_l and wavelength λ_l for $E_b \gg 1$ keV. If the target material is known, good estimations of the surface properties can be obtained by employing high-energy electron beams and lasers. However, accurate simulations or closed-loop sensing algorithms are needed to account for backscattered electrons, reflected photons, and, for materials with high yields at high impact energies (e.g. gold), secondary electrons. The exact same approach could be employed in combination with spacecraft charging models to set the target potential to a certain value. This may find application in the electrostatic tractor concept [11].

C. Material identification

The photoelectric effect has been traditionally employed to determine the work function of surfaces in laboratory settings. The material is exposed to a coherent laser beam with predefined wavelength, and the energy of the emitted photoelectrons is characterized with an RPA. The stopping potential, defined as the value that matches the energy of photoelectrons and prevents their collection at the RPA, is obtained. This process is repeated for lasers of various energies, leading to a stopping potential versus laser photon energy plot. Following Eq. 16, the y-intercept is the work function of the material [49]. From a remote sensing perspective, the value of the work function

TABLE II
KEY PARAMETERS OF COMMERCIAL-OFF-THE-SHELF UV LASERS

Model	Divergence (mrad)	λ_l (nm)	ω_l (eV)	P_l (mW)
TOPTICA Photonics CW213	1	190	6.5	20
Photon Systems HeAg-224SL	4	224.3	5.5	50
Opto Engine LLC MPL-N-257	1	257	4.8	15
Photon Systems NeCu 30-248	4	248	5	50

can be employed to constrain the range of possible surface materials.

The same process could be utilized to approximately characterize the materials employed at the surface of a target spacecraft. The servicer would utilize UV lasers of varying wavelengths to excite photoelectrons, which are then received by an RPA. The stopping potential is thus determined, and with it, the work function of the material. However, the flux of photoelectrons arrives at the servicer with an energy equal to the potential difference between the crafts plus the stopping potential. Given that the work function is of the order of 5 eV (see Table I) and that the maximum touchless potential sensing accuracy achieved to date is of the order of 20 V [2], uncertainties in the stopping potential determination may render this approach unfeasible. Instead, multiple lasers with energies between 2 and 10 eV could be employed to sequentially excite the target. The minimum energy that produces a peak in the energy spectrum would become the closest approximation of the work function of the material. As shown in Sec. IV-A this peak would also match the potential difference between the crafts. Enhanced sensitivities are achieved by operating the RPA in derivative mode.

D. Implementation notes

Ultraviolet lasers pass a long-wavelength laser through nonlinear crystals, which reduce the wavelength to the desired value. Tunable and fixed-wavelength technologies are used in Raman spectroscopy, photoemission spectroscopy, or photoluminscence, among others [50]. Examples of commercial lasers that could potentially be employed in the applications discussed in this work are presented in Table II with their specifications. However, they need to be adapted for use in space. This would also find application in different fields. For instance, high output-power (several kW) space-based lasers have been proposed to ablate and induce a kinetic impulse on target debris, altering its trajectory [51, 52].

V. CONCLUSIONS

The combined use of UV lasers and energetic electron beams for photoelectron and x-ray generation is revealed as a robust hybrid remote potential sensing method. This approach overcomes the technical challenges of previous electron-based approaches by minimizing or eliminating multiple sources of uncertainty. In particular, the effect of the electrostatic environment on low-energy electron beams and the degradation induced by surface contamination. New approaches to neutral potential sensing, touchless charge control, and material identification are proposed. UV lasers can also be employed as standalone elements in these aplications. A comparison of active potential sensing methods is finally presented in Table III.

ACKNOWLEDGEMENTS

This work was supported by U.S. Air Force Office of Scientific Research under grant FA9550-20-1-0025 and the Rafael del Pino Foundation under its 2021 Excellence Fellowship. The authors thank Dr. Kieran Wilson for his comments on the manuscript.

REFERENCES

[1] M. T. Bengtson, K. T. Wilson, and H. Schaub, "Experimental results of electron method for remote spacecraft charge sensing," *Space Weather*, vol. 18, no. 3, pp. 1–12, 2020.

[2] Álvaro Romero Calvo, J. Hammerl, and H. Schaub, "Touchless potential sensing of complex differentially-charged shapes using secondary electrons," in *AIAA SCITECH 2022 Forum*, 2022.

[3] K. T. H. Wilson and H. Schaub, "X-ray spectroscopy for electrostatic potential and material determination of space objects," *IEEE Transactions on Plasma Science*, vol. 47, no. 8, pp. 3858–3866, Aug. 2019.

[4] K. T. Wilson, M. T. Bengtson, and H. Schaub, "X-ray spectroscopic determination of electrostatic potential and material composition for spacecraft: Experimental results," *Space Weather*, vol. 18, no. 4, p. e2019SW002342, 2020.

[5] K. Wilson and H. Schaub, "Impact of electrostatic perturbations on proximity operations in high earth orbits," *Journal of Spacecraft and Rockets*, vol. 58, no. 5, pp. 1293–1302, 2021.

[6] K. Wilson, A. Romero-Calvo, and H. Schaub, "Constrained guidance for spacecraft proximity operations under electrostatic perturbations," *Journal of Spacecraft and Rockets*, vol. 0, no. 0, pp. 1–13, 2022, *in press*.

[7] H. Schaub, G. G. Parker, and L. B. King, "Challenges and prospects of coulomb spacecraft formation control," *The Journal of the Astronautical Sciences*, vol. 52, no. 1, pp. 169–193, Mar 2004.

[8] F. Casale, H. Schaub, and J. D. Biggs, "Lyapunov optimal touchless electrostatic detumbling of geostationary debris using surface multisphere models," *AIAA Journal of Spacecraft and Rockets*, vol. 58, no. 3, 2021.

[9] H. Schaub and D. F. Moorer, "Geosynchronous large debris reorbiter: Challenges and prospects," *The Journal of the Astronautical Sciences*, vol. 59, no. 1, pp. 161–176, Jun 2012.

[10] J. Hughes and H. Schaub, "Prospects of using a pulsed electrostatic tractor with nominal geosynchronous conditions," *IEEE Transactions on Plasma Science*, vol. 45, no. 8, pp. 1887–1897, 2017.

[11] M. Bengtson, K. Wilson, J. Hughes, and H. Schaub, "Survey of the electrostatic tractor research for reorbiting passive geo space objects," *Astrodynamics*, vol. 2, no. 4, pp. 291–305, Dec 2018.

[12] J. A. Hughes and H. Schaub, "Electrostatic tractor analysis using a measured flux model," *Journal of Spacecraft and Rockets*, vol. 57, no. 2, pp. 207–216, 2020.

[13] J. Hammerl and H. Schaub, "Effects of electric potential uncertainty on electrostatic tractor relative motion control equilibria," *Journal of Spacecraft and Rockets*, vol. 59, no. 2, pp. 552–562, 2022.

[14] K. Wilson, M. Bengtson, and H. Schaub, "Remote electrostatic potential sensing for proximity operations: Comparison and fusion of methods," *Journal of Spacecraft and Rockets*, 2022, *under review*.

[15] A. Romero-Calvo, G. Cano-Gómez, and H. Schaub, "Simulation and uncertainty quantification of electron beams in active spacecraft charging scenarios," *Journal of Spacecraft and Rockets*, 2021, *in press*.

[16] S. T. Lai, *Fundamentals of Spacecraft Charging: Spacecraft Interactions with Space Plasmas*. Princeton University Press, 2012.

[17] N. L. Sanders and G. T. Inouye, "Secondary emission effects on spacecraft charging: Energy distribution considerations," *Spacecraft Charging Technology*, pp. 747–755, 1978, nASA-2071, ADA-084626.

[18] J. Christensen, "Electron Yield Measurements of High-Yield, Low-Conductivity Dielectric Materials," Ph.D. dissertation, Utah State University, 2017.

[19] E. H. Darlington and V. E. Cosslett, "Backscattering of 0.5-10 kev electrons from solid targets," *Journal of Physics D: Applied Physics*, vol. 5, no. 11, pp. 1969–1981, nov 1972.

[20] M. S. Chung and T. E. Everhart, "Simple calculation of energy distribution of low-energy secondary electrons emitted from metals under

TABLE III
COMPARISON OF ACTIVE SENSING METHODS

Method	Advantages	Disadvantages
Secondary Electrons (SE's)	- Most accurate (10s of V) - Favored by low-energy electron beams	- Beam sensitive to the electrostatic environment - Detectability dependent on system geometry - Long RPA sampling time
X-Ray	- Detectability weakly dependent on location wrt target - Low x-ray sensor sampling time - Energetic beam stabilizes backscattered electron yield - Reduced influence of surface contamination - Enables material identification	- High uncertainty (100s of V) - Requires energetic electron beams
UV Laser	- Most accurate (10s of V) - Laser independent to electrostatic environment - Observable and controllable - Enables material identification	- Generally, lower currents involved - Not suitable for positive target potentials
Combined SE's and X-Ray	- Currently most robust and accurate method - Possible to obtain signals from most angles wrt target	- Each method benefits from different beam energies - Target charge balance subject to high uncertainty
Combined UV Laser and X-Ray	- Allows optimum electron beam and photon energies - Enables charge control - Enables material identification	- Complex hardware (leading, possibly, to larger mass/volume)

electron bombardment," *Journal of Applied Physics*, vol. 45, no. 2, pp. 707–709, 1974.
[21] H. Bruining, *Physics and Applications of Secondary Electron Emission*. New York: McGraw-Hill Book Co., Inc. London: Pergamon Press Ltd., 1954, chapter 7: Theory of Secondary Electron Emission; Discussion of Some Properties of Secondary Electrons.
[22] T. E. Everhart, "Simple theory concerning the reflection of electrons from solids," *Journal of Applied Physics*, vol. 31, no. 8, pp. 1483–1490, 1960.
[23] J. Jeanneret, "Photoemission in lhc - a simple model," CERN, Tech. Rep. Note 97-48 (AP), 1997.
[24] C. J. POWELL, "Analysis of optical- and inelastic-electron-scattering data. iii. reflectance data for beryllium, germanium, antimony, and bismuth," *J. Opt. Soc. Am.*, vol. 60, no. 2, pp. 214–220, Feb 1970.
[25] S. Lai and M. Tautz, "Aspects of spacecraft charging in sunlight," *IEEE Transactions on Plasma Science*, vol. 34, no. 5, pp. 2053–2061, 2006.
[26] H. Bennett and J. Porteus, "Relation between surface roughness and specular reflectance at normal incidence," *JOSA*, vol. 51, no. 2, pp. 123–129, 1961.
[27] S. T. Lai, "Charging of mirror surfaces in space," *Journal of Geophysical Research: Space Physics*, vol. 110, no. A01204, 2005.
[28] R. E. Van Grieken and A. A. Markowicz, *Handbook of X-Ray Spectrometry*. Marcel Dekker Inc., 2001, second Edition.
[29] J. Trincavelli and G. Castellano, "The prediction of thick target electron bremsstrahlung spectra in the 0.25–50 kev energy range," *Spectrochimica Acta Part B: Atomic Spectroscopy*, vol. 63, no. 1, pp. 1–8, 2008.
[30] G. Castellano, J. Osán, and J. Trincavelli, "Analytical model for the bremsstrahlung spectrum in the 0.25–20 kev photon energy range," *Spectrochimica Acta Part B: Atomic Spectroscopy*, vol. 59, no. 3, pp. 313–319, 2004.
[31] K. T. Wilson, "Remote electrostatic potential determination for spacecraft relative motion control," Ph.D. dissertation, Aerospace Engineering Sciences Department, University of Colorado, Boulder, CO, 2021.
[32] D. Laguitton and W. Parrish, "Experimental spectral distribution versus kramers' law for quantitative x-ray fluorescence by the fundamental parameters method," *X-Ray Spectrometry*, vol. 6, no. 4, pp. 201–203, 1977.
[33] L. Olano and I. Montero, "Energy spectra of secondary electrons in dielectric materials by charging analysis," *Results in Physics*, vol. 19, p. 103456, 2020.
[34] D. R. Lide, *CRC Handbook of Chemistry and Physics: 84th Edition*. CRC Press, 2003.
[35] R. C. Hoffmann, "Electron-Induced Electron Yields of Uncharged Insulating Material," Ph.D. dissertation, Physics Department, Utah State University, 2010.
[36] A. Assa and M. El Gomati, "Backscattering coefficients for low energy electrons," *Scanning Microscopy*, vol. 12, no. 1, pp. 185–192, 1998.
[37] B. Feuerbacher and B. Fitton, "Experimental investigation of photoemission from satellite surface materials," *Journal of Applied Physics*, vol. 43, no. 4, pp. 1563–1572, 1972.
[38] K. Kawasaki, S. Inoue, E. Ewang, K. Toyoda, and M. Cho, "Measurement of electron emission yield by electrons and photons for space aged material," in *Proceedings of the 14th Spacecraft Charging Technology Conference, ESA/ESTEC Noordwijk, Netherlands*, 2016, pp. 1–7.
[39] H. Rodriguez, K. Abercromby, M. Mulrooney, and E. Barker, "Optical properties of multi-layered insulation," NASA, Tech. Rep., 2007.
[40] J. B. Heaney, "Evaluation of commercially supplied silver coated teflon for spacecraft temperature control usage," NASA, Tech. Rep. TM-X-70488, 1974.
[41] V. Baglin, J. Bojko, O. Gröbner, B. Henrist, N. Hilleret, C. Scheuerlein, and M. Taborelli, "The secondary electron yield of technical materials and its variation with surface treatments," in *Proceedings of EPAC 2000, Vienna, Austria*, 2000.
[42] S. Robertson, Z. Sternovsky, and B. Walch, "Reduction of asymmetry transport in the annular penning trap," *Physics of Plasmas*, vol. 11, no. 5, pp. 1753–1756, 2004.
[43] C. Jin, A. Ottaviano, and Y. Raitses, "Secondary electron emission yield from high aspect ratio carbon velvet surfaces," *Journal of Applied Physics*, vol. 122, no. 17, p. 173301, 2017.
[44] M. F. Diaz-Aguado, J. W. Bonnell, S. D. Bale, S. J. Rezvani, K. Koshmak, A. Giglia, S. Nannarone, and M. Gruntman, "Experimental investigation of total photoemission yield from new satellite surface materials," *Journal of Spacecraft and Rockets*, vol. 56, no. 1, pp. 248–258, 2019.
[45] J. A. Reyes, K. W. Fulford, E. A. Plis, R. C. Hoffmann, V. J. Murray, H. M. Cowardin, D. Cone, D. C. Ferguson, M. T. Bengtson, J. R. Shah, and D. P. Engelhart, "Spectroscopic behavior of various materials in a geo simulated environment," *Acta Astronautica*, vol. 189, pp. 576–583, 2021.
[46] R. B. Torbert, H. Vaith, M. Granoff, M. Widholm, J. A. Gaidos, B. H. Briggs, I. G. Dors, M. W. Chutter, J. Macri, M. Argall, D. Bodet, J. Needell, M. B. Steller, W. Baumjohann, R. Nakamura, F. Plaschke, H. Ottacher, J. Hasiba, K. Hofmann, C. A. Kletzing, S. R. Bounds, R. T. Dvorsky, K. Sigsbee, and V. Kooi, "The electron drift instrument for mms," *Space Science Reviews*, vol. 199, no. 1, pp. 283–305, Mar 2016.
[47] M. T. Bengtson and H. Schaub, "Electron-based touchless potential sensing of shape primitives and differentially-charged spacecraft," *Journal of Spacecraft and Rockets*, vol. 58, no. 6, pp. 1847–1857, Nov. – Dec. 2021.
[48] K. Wilson, Álvaro Romero-Calvo, M. Bengtson, J. Hammerl, J. Maxwell, and H. Schaub, "Development and characterization of the eclips space environments simulation facility," *Acta Astronautica*, vol. 194, pp. 48–58, 2022.
[49] R. Powell, "Photoelectric effect: Back to basics," *American Journal of Physics*, vol. 46, no. 10, pp. 1046–1051, 1978.
[50] S. jin Zhang, D. fu Cui, F. feng Zhang, Z. Xu, Z. min Wang, F. Yang, N. Zong, W. Tu, Y. Chen, H. yan Xu, F. liang Xu,

Q. jun Peng, X. yang Wang, C. tian Chen, and Z. yan Xu, "High power all solid state vuv lasers," *Journal of Electron Spectroscopy and Related Phenomena*, vol. 196, pp. 20–23, 2014, advances in Vacuum Ultraviolet and X-ray Physics, The 38th International Conference on Vacuum Ultraviolet and X-ray Physics (VUVX2013), University of Science and Technology of China. [Online]. Available: https://www.sciencedirect.com/science/article/pii/S036820481400036X

[51] S. Shen, X. Jin, and C. Hao, "Cleaning space debris with a space-based laser system," *Chinese Journal of Aeronautics*, vol. 27, no. 4, pp. 805–811, 2014.

[52] Q. Wen, L. Yang, S. Zhao, Y. Fang, Y. Wang, and R. Hou, "Impacts of orbital elements of space-based laser station on small scale space debris removal," *Optik*, vol. 154, pp. 83–92, 2018.